A bis-vanadyl coordination complex as a two-qubit quantum gate

Ivana Borilovic,[a] Pablo J. Alonso,[b] Olivier Roubeau[b,*] and Guillem Aromí [a,c,*]

SUPPORTING INFORMATION

Synthesis

Solvents and reagents were used as received from the commercial suppliers in preparation of ligands and compounds. An exception was only made for Claisen condensation reactions, where anhydrous THF (PureSolv Micro Solvent Purification Systems) was used as solvent to avoid any hydrolysis as possible side reaction. Sodium hydride was applied as a suspension in mineral oil (60% w/w) which was purified by washing with hexanes under nitrogen and posterior extraction of solvent by filter cannula. Tetrabutylammonium hydroxide was employed as a solution in methanol (c=1 mol/dm^3), while vanadyl sulfate and titanyl acetylacetonate were used as hydrated and anhydrous salt, respectively ($VOSO_4 \cdot xH_2O$ and $[(TiO)(C_5H_7O_2)_2]$).

Synthesis of 1,6-bis-(2-hydroxyphenyl)-1,3,4,6-hexanetetraone (H_4L1). Sodium hydride (4.47 g, 111.8 mmol) was suspended with stirring for 10 minutes under nitrogen in hexane (80 mL), and then the solvent was extracted with a filter cannula. This procedure was repeated and to the resulting white solid was then added dry THF (100 mL). In a separate Schlenk flask, 2-hydroxyacetophenone (6.92 g, 50.8 mmol) was dissolved under nitrogen in dry THF (50 mL) and then added dropwise to the suspension of NaH in THF. This caused the yellow-green colouring of the reaction mixture and evolution of hydrogen. When the addition was complete, the resulting suspension was further stirred for 15 min at room temperature, to which followed the addition of dimethyl oxalate (3.00 g, 25.4 mmol) dissolved in THF (50 mL). The reaction was then carefully brought to reflux, exerting caution to the abrupt hydrogen evolution occurring when the temperature reaches 50 °C, which is accompanied by a sudden change to orange colour of the reaction mixture. After 12 h of reflux, the orange suspension was allowed to cool to room temperature and the THF was removed under reduced pressure. The orange-red solid obtained was then dissolved in water and acidified with HCl(aq) to pH=3. The yellow-brown solid precipitated was collected by filtration and purified by recrystallisation from acetone (average yield 2.60 g, 31%). ^{1}H NMR (400 MHz, $CDCl_3$), δ(ppm): 6.97 (t, 2H, -Ar-*H*), 7.03 (d, 2H, -Ar-*H*), 7.15 (s, 2H, -COC*H*COH), 7.53 (t, 2H, -Ar-*H*), 7.84 (d, 2H, -Ar-*H*), 11.92 (s, 2H, Ar-O*H*), 14.17 (s, 2H, -O*H*enol). ESI MS: m/z $[H_3L1]^-$ = 325.07. IR (KBr pellet) ν/cm^{-1}: 3420 b, 3114 s, 3049 b, 1625 s, 1598 s, 1575 s, 1489 s, 1442 s, 1404 b, 1334 s, 1301 s, 1265 s, 1205 s, 1163 s, 1130 s, 1106 s, 1034 s, 848 s, 832 s, 812 s, 760 s, 741 s, 704 s, 684 b, 602 s, 531 w, 507 s, 477 w, 425 w.

Synthesis of 5,5'-bis-(2-hydroxyphenyl)-3,3'-bis-pyrazole (H_4L). Ligand **H_4L1** (1.50 g, 4.60 mmol) was suspended in methanol (50 mL). To this yellow suspension was added hydrazine monohydrate (46 mmol, 2.23 mL), which caused the immediate dissolution of all solids and a color fading. The mixture was brought to reflux and the latter was maintained for 14 h. During the first

hour of the reaction, the precipitation of white solid was observed. Upon completion of the reaction, the mixture was allowed to cool to room temperature, which resulted in the extensive precipitation of the product **H_4L**. Typical yields of 55 % (0.81 g) were obtained. An additional crop of the product can be collected after reduction of the solvent volume to half (additional 8%, 0.12 g). Single crystals can be obtained directly from the reaction mixture or by recrystallization from acetone. ^{1}H NMR (400 MHz, d_6-Acetone), δ(ppm): 6.96 (d, 2H, -Ar-*H*), 7.24 (t, 2H, -Ar-*H*), 7.75 (s, 1H, -Ar-*H*), 10.85 (broad s, Ar-O*H*), 12.90 (broad s, Ar-N*H*); 1H NMR (400 MHz, *d*6-DMSO), δ(ppm): 6.91 (t, 1H, -Ar-*H*), 6.96 (d, 1H, -Ar-*H*), 7.16 (s, 1H, -Ar-*H*), 7.19 (t, 1H, -Ar-*H*), 7.73 (d, 1H, -Ar-*H*). ESI MS: *m*/*z* [H_4L4+H^+] = 319.12, [H_4L4+Na^+] = 341.10. IR (KBr pellet) *v*/cm^{-1}: 3415 s, 3186 b, 3149 b, 3051 b, 2919 b, 1587 s, 1554 s, 1516 s, 1508 s, 1463 s, 1392 s, 1348 s, 1287 s, 1252 s, 1169 s, 1115 s, 1066 s, 1045 s, 1015 s, 969 s, 932 s, 825 s, 784 s, 741 s, 702 s, 679 s, 663 s, 647 s, 614 s, 564 s, 540 s, 478 s, 466 s. EA (%): Calc. (Found for $C_{18}H_{14}N_4O_2$): C 67.92 (68.06); H 4.43 (4.37); N 17.60.

Synthesis of $(Bu_4N)_2[(VO)_2(HL)_2]$ (1). Tetrabutylammonium hydroxide in 1 M MeOH solution (380 µL, 0.380 mmol) was added to a colorless pyridine solution of **H_4L** (30.0 mg, 0.094 mmol in 10 mL) causing an immediate change of color to light yellow. The resulting solution was stirred for 10 min and then was added dropwise to the hot pyridine solution of $VOSO_4{\cdot}xH_2O$ (34.1 mg, 0.188 mmol), the latter changing its color from blue to violet. The solution obtained was stirred for 1h at room temperature, filtered and layered with Et_2O. Violet blocks appeared overnight and these were allowed to grow until the diffusion was complete (approximately over 10 days). The yield was 68 % (40 mg). ESI-MS, m/z = 382.0. IR (KBr pellet) *v*/cm^{-1}: 3430 b, 3052 b, 2959 s, 2932 b, 2872 s, 1596 s, 1560 s, 1482 s, 1458 s, 1440 s, 1379 s, 1347 s, 1312 s, 1299 s, 1268 s, 1251 s, 1151 s, 1118 s, 1062 s, 1035 s, 975 s, 933 s, 878 s, 855 s, 785 s, 748 s, 697 s, 669 s, 635 s, 620 s, 576 s, 529 s, 504 s. While single crystals contain crystallization pyridine molecules, these are lost and exchanged with air moist upon exposure to air. EA (%): Calc. (Found for $C_{68}H_{94}N_{10}O_6V_2{\cdot}1.1H_2O$): C, 64.35 (64.62); H, 7.64 (7.92); N, 11.04 (11.07).

Synthesis of $(Bu_4N)_2[(TiO)_2(HL)_2]$ (2). Tetrabutylammonium hydroxide in 1 M MeOH solution (380 µL, 0.380 mmol) was added to a colorless pyridine solution of **H_4L** (30.0 mg, 0.094 mmol in 10 mL) causing an immediate change of color to light yellow. The resulting solution was stirred for 10 min and then was added dropwise to a hot pyridine (110 ºC) solution of $TiO(acac)_2$ (49.4 mg, 0.188 mmol), the latter changing its color from clear to bright yellow . The solution obtained was stirred for 1h at room temperature, filtered and layered with Et_2O. Light-yellow blocks were recovered after 3 weeks in a yield of *ca.* 30 %. EA (%): Calc. (Found for $C_{68}H_{94}N_{10}O_6Ti_2$): C, 65.70 (65.69); H, 7.34 (7.62); N, 11.21 (11.27).

A different polymorph **2'** of the same compound crystallizes using the same procedure, albeit with defect of $TiO(acac)_2$ (37.0 mg, 0.141 mmol). In this case, light-yellow plates appeared few days after layering, and were allowed to grow until the system was homogeneous (approximately 10 days). The yield was 34% (20 mg).

IR (KBr pellet) *v*/cm^{-1}: 3434 b, 3054 b, 2956 s, 2933 b, 2873 s, 1595 s, 1563 s, 1483 s, 1459 s, 1441 s, 1381 s, 1344 s, 1310 s, 1299 s, 1270 s, 1249 s, 1150 s, 1118 s, 1060 s, 1037 s, 984 ws, 946 s, 864 s, 783 s, 750 s, 697 s, 670 s, 630 s, 581 s, 565 s, 514 s, 500 s.
Contrary to its vanadyl analogue, all attempts to detect the $[(TiO)_2(HL)_2]^{2-}$ complex through mass spectrometry were unsuccessful.

Attempted *direct* synthesis of $(TBA)_2[(TiO)_{2-2x}(VO)_{2x}(HL_1)_2]$.
Tetrabutylammonium hydroxide (380 µL, 0.380 mmol) was added to the colourless pyridine solution of **H_4L** (30.0 mg, 0.094 mmol in 10 mL) causing its immediate change of colour to light yellow. The obtained solution was stirred for 10 min and then was added dropwise to a pyridine solution of $TiO(acac)_2$ (37.0 mg, 0.188 mmol) and $VOSO_4 \cdot xH_2O$ (8.5 mg, 0.047 mmol), changing its colour from blue-green to yellow-gold. The resulting solution was stirred for 1h at room temperature, filtered and layered with Et_2O. Yellow-blue plates appeared after few days and were allowed to grow until the system was homogenous (approximately 10 days). Average yield was 39 % (23.0 mg). Mass spectrometry however indicates the presence of two forms of the heterometallic complex at m/z = 380.5 ($[(VO)(TiO)(HL)_2]^{2-}$) and 388.5 ($[(VO)(TiO)(OH)(HL)(L)]^{2-}$) in addition to the homometallic $[(VO)_2(HL)_2]^{2-}$ complex at m/z = 382.0. The absence of any fragment from the homometallic $[(TiO)_2(HL)_2]^{2-}$ is consistent with observations on the pure complexes **2** and **2'**. Altogether, this likely indicates the formation of a mixture of the three possible complexes.

Synthesis of $(Bu_4N)_2[(TiO)_{2-2x}(VO)_{2x}(HL)_2]$ (3, x≈0.1) from its pre-crystallized components. Single crystals of compounds **1** (5 mg, 0.00400 mmol) and **2'** (50 mg, 0.0402 mmol) were dissolved in 12 mL of pyridine giving yellow-gold solution. The mixture was stirred for 30 min at room temperature, filtered and layered with Et_2O. Light yellow plates (with some violet reflects depending on light and orientation of the crystals) appeared after few hours and were allowed to grow until the system was homogenous (approximately 10 days). Average yield was 53 % (29.0 mg). IR (KBr pellet) *v*/cm^{-1}: 3428 b, 3049 b, 2958 s, 2933 b, 2871 s, 1595 s, 1564 s, 1485 s, 1460 s, 1440 w, 1382 s, 1346 s, 1312 s, 1302 s, 1271 s, 1250 s, 1150 s, 1119 s, 1061 s, 1036 s, 983 ws, 946 s, 936 bw, 865 s, 783 s, 755 s, 697 s, 670 s, 631 s, 620 s, 580 s, 567 s, 513 s, 500 s. While single crystals contain crystallization pyridine molecules, these are lost and exchanged with air moist upon exposure to air. EA (%): Calc. (Found for $C_{68}H_{94}N_{10}O_6Ti_2 \cdot 7H_2O$): C 59.64 (59.30); H 7.95 (7.73); N 10.23 (10.09). The presence of the homometallic vanadyl $[(VO)_2(HL)_2]^{2-}$ complex is confirmed by mass spectrometry (ESI, m/z = 382.0), while, as for the pure **2** and **2'**, all attempts to detect the $[(TiO)_2(HL)_2]^{2-}$ complex through mass spectrometry were unsuccessful.

Single Crystal X-ray Diffraction (SCXRD).

Data for the ligand H_4L crystallized from its mother liquor with half hydrazine molecule **$H_4L \cdot 0.5N_2H_4$** and for compound **1** were obtained at 100 K on a Bruker APEX II CCD diffractometer at the Advanced Light Source beam-line 11.3.1 at Lawrence Berkeley National Laboratory, from a silicon 111 monochromator (λ = 0.77490 Å), respectively on a colourless needle of dimensions 0.26 x 0.20 x 0.07 mm^3 and a violet block of dimensions 0.18 x 0.03 x 0.02 mm^3. Data for compound **2** were obtained on a light yellow block of dimensions 0.08 x 0.07 x 0.04 mm^3 at 100 K on the BL13-XALOC beamline[1] of the ALBA synchrotron (λ = 0.77490 Å). Data for **2'** and **3** were collected at 100 K on a Bruker APEXII QUAZAR diffractometer equipped with a microfocus multilayer monochromator with MoKa radiation (λ = 0.71073 Å) respectively on a light yellow plate of dimensions 0.27 x 0.07 x 0.07 mm^3 and a light yellow-violet block with dimensions 0.09 x 0.07 x 0.06. Data reduction and absorption corrections were performed with SAINT and SADABS, respectively,[2] except for compound **2** for which data reduction was done using CrysalisPro[3] and no absorption corrections were applied. The structures were solved by intrinsic phasing with SHELXT.[4] All four structures were refined by full-matrix least-squares on F^2 with SHELXL.[5] In the case of **3**, the final structure was refined as a 100% titanyl compound, because refinement with heterometallic composition did not converge satisfactorily. One likely reason for this is that in both structures of **1** and **3**, the vanadyl/titanyl sites are disordered over two opposite orientations, although there is one main component with >95 % occupancy. The Ti-O and Ti-N bond lengths in the structure of **3** are in fact intermediate between those of **1** and **2**, thus in agreement with a heterometallic composition.

All details can be found in CCDC 1962565-1962566-1969357-1962567-1962568 (**$H_4L \cdot 0.5N_2H_4$-1-2-2'-3**) that contain the supplementary crystallographic data for this paper. These data can be obtained free of charge from The Cambridge Crystallographic Data Center via https://summary.ccdc.cam.ac.uk/structure-summary-form. Crystallographic and refinement parameters are summarized in Table S1. Selected bond lengths and intermolecular distances are given in Tables S2 and S3.

Table S1. Crystallographic and refinement parameters for the structures of compounds **$H_4L\cdot0.5N_2H_4$**, **$(TBA)_2[(VO)_2(HL)_2]\cdot4.5py$** (**1**), **$(TBA)_2[(TiO)_2(HL)_2]$** (**2** and **2'**) and **$(TBA)_2[(MO)_2(HL)_2]\cdot4py$** (**3, M=Ti:V**). Note that the later was refined with M=Ti, because a refinement including an heterometallic composition did not converge satisfactorily.

Compound	**$H_4L\cdot0.5N_2H_4$**	**1**	**2**	**2'**	**3**
Formula	$C_{18}H_{16}N_5O_2$	$C_{90.5}H_{116.5}N_{14.5}O_6V_2$	$C_{68}H_{94}N_{10}O_6Ti_2$		$C_{88}H_{114}N_{14}O_6Ti_2$
FW (g mol^{-1})	334.36	1605.36	1243.33		1559.73
Wavelength (Å)	0.7749	0.7749	0.7749	0.71073	0.71073
T (K)	100	100	100	100	100
Crystal system	monoclinic	triclinic	triclinic	monoclinic	triclinic
Space group	*C*2/c	*P*–1	*P*–1	$P2_1/n$	*P*–1
a (Å)	28.460(7)	12.8070(10)	9.9438(4)	12.3192(8)	12.7936(6)
b (Å)	4.9320(11)	18.384(2)	12.8964(10)	17.5994(11)	18.1210(10)
c (Å)	24.318(6)	20.411(2)	13.5489(6)	14.9947(8)	19.6033(10)
α (°)	90	73.0220(10)	86.435(5)	90	98.602(3)
β (°)	112.810(9)	72.779(2)	79.518(4)	96.710(4)	108.452(3)
γ (°)	90	70.673(2)	74.129(5)	90	101.429(3)
V (Å^3)	3146.4(13)	4230.0(7)	1643.24(17)	3228.7(3)	4113.9(4)
Z	8	2	1	2	2
ρ_{calcd} (g cm^{-3})	1.412	1.260	1.256	1.279	1.259
μ (mm^{-1})	0.116	0.354	0.376	0.307	0.256
Reflections	4283	19299	6528	5976	16760
R_{int}	0.0574	0.0847	0.0249	0.0791	0.0665
Restraints	10	136	733	0	50
Parameters	259	1105	542	395	1013
S	1.035	1.034	1.044	1.042	1.066
R_1 [$I>2\sigma(I)$]	0.0514	0.0851	0.1166	0.0659	0.0772
wR_2 [$I>2\sigma(I)$]	0.1369	0.2503	0.3285	0.1396	0.2171
R_1 [all data]	0.0618	0.1008	0.1203	0.1040	0.1167
wR_2 [all data]	0.1454	0.2679	0.3350	0.1571	0.2489
Largest peak / hole (*e* Å^3)	0.353 / –0.255	0.975 / –0.597	1.423 / –1.909	0.926 / –0.593	1.080 / –0.724

Table S2. Intramolecular metal···metal separations and bond lengths (Å) describing the coordination environments of the metal sites in the structures of compounds **1**, **2** and **3**. Note that for the later, refinement was done with M=Ti, because a refinement including an heterometallic composition did not converge satisfactorily. The bond lengths are however clearly in between those for **1** and **3**, supporting the heterometallic composition of **3**.

	1 (M=V)	**2 (M=Ti)**	**2' (M=Ti)**	**3 (M=Ti)**
M1–O1	1.6021(18)	1.643(3)	1.644(3)	1.640(2)
M1–O2	1.9169(18)	1.913(3)	1.897(2)	1.915(2)
M1–O3 (O5)*	1.9334(18)	1.902(3)	1.914(2)	1.905(2)
M1–N1	2.0874(19)	2.189(4)	2.185(3)	2.167(3)
M1–N4 (N5)*	2.087(2)	2.178(3)	2.179(3)	2.156(3)
M2–O4	1.5997(18)			1.637(2)
M2–O5 (O3)*	1.9125(19)			1.902(2)
M2–O6	1.9503(19)			1.916(2)
M2–N5 (N4)*	2.088(2)			2.152(3)
M2–N8	2.095(2)			2.171(3)
M···M **	8.279(2)/8.255(2)	8.511(2)	8.538(2)	8.466(2)

* in the case of **3**, the asymmetric unit consist of one full molecule, while in the case of **1**, there are two half molecules, resulting in few differences in the atomic numbering

** V1···V1#1/V2···V2#1, Ti1···Ti1#1 and Ti1···Ti2 respectively for **1**, **2/2'** and **3**, with symmetry operations #1 = -x, 1-y, 2-z, #2 = 1-x, 1-y, 1-z and #3 = -x, -y, 1-z

Table S3. Distances and angles describing the hydrogen bonds in the structures of compounds **$H_4L \cdot 0.5N_2H_4$**, **1**, **2** and **3**.

D–H···A	D–H (Å)	H···A (Å)	D···A (Å)	D–H···A (º)
$H_4L \cdot 0.5N_2H_4$				
O1–H1···N5	0.99(2)	1.82(2)	2.773(4)	159.4(19)
O1–H1···N6	0.99(2)	1.70(2)	2.689(3)	177(2)
O2–H2···N4	0.95(2)	1.79(2)	2.6280(16)	145.0(18)
N1–H1N···O1	0.89(2)	2.175(19)	2.6814(16)	115.7(15)
N3–H3N···N2#1	0.886(19)	2.065(19)	2.9001(17)	156.7(16)
N5–H5A···O1#2	0.95(2)	2.26(3)	3.087(4)	146(4)
N5–H5B···O2#1	0.913(19)	1.88(2)	2.765(3)	164(4)
N6–H6A···O1#2	0.96(2)	2.45(3)	3.344(4)	156(5)
N6–H6B···O2#3	0.969(19)	2.12(3)	3.017(4)	154(4)
1				
N3–H3···N2	0.88	1.85	2.614(3)	143.4
N7–H7···N6	0.88	1.85	2.604(3)	142.9
2				
N2–H2B···N3	0.88	1.86	2.619(4)	143.1
2'				
N2–H2···N3	0.88(4)	1.79(4)	2.598(4)	153(4)
3				
N2–H6···N6	0.86(4)	1.85(4)	2.603(4)	146(4)
N7–H7···N3	0.79(4)	1.92(4)	2.610(4)	147(4)

#1: -x, 1-y, 1-z; #2: x, 1+y, z; #3: x, 1-y, z-0.5

Magnetic properties.

Variable-temperature magnetic susceptibility data were obtained with a MPMS-XL SQUID magnetometer at the Unitat de Mesures Magnètiques of the Universitat de Barcelona. *ac* susceptibility measurements were performed with a commercial MPMS-XL SQUID magnetometer and the ACMS option of a commercial Physical Properties Measurement System (PPMS), both hosted by the Physical Measurements Unit of the Servicio General de Apoyo a la Investigación-SAI, Universidad de Zaragoza. Samples were in all cases crystalline and not previously subjected to vacuum drying. The data were corrected for the contribution of the capsule sample holder, determined empirically. The sample diamagnetic contributions to the susceptibility were corrected using Pascal's constant tables. Direct current (*dc*) data were collected at variable temperature between 2 and 300 K with an applied field of 1000 Oe, as well as at 2 K at variable *dc* fields up to 5 T. Isothermal alternating current (*ac*) data were collected with a 4 Oe field oscillating at different frequencies in the range $1 \leq \nu \leq 10.000$ Hz. Measurements were performed at 2 K at various applied *dc* fields in the range 0-20000 Oe, and then at 3000 Oe at various temperatures up to 20 K.

The spin-lattice relaxation time T_1^{ac} or τ was extracted from the frequency dependence of the real and imaginary components of the *ac* susceptibility χ and χ" using the following expressions corresponding to the generalized Debye model:

$$\chi'(\omega) = \chi_S + (\chi_T - \chi_S)\frac{1 + (\omega\tau)^\beta \cos\left(\frac{\pi\beta}{2}\right)}{1 + 2(\omega\tau)^\beta \cos\left(\frac{\pi\beta}{2}\right) + (\omega\tau)^{2\beta}}$$

$$\chi''(\omega) = (\chi_T - \chi_S)\frac{(\omega\tau)^\beta \sin\left(\frac{\pi\beta}{2}\right)}{1 + 2(\omega\tau)^\beta \cos\left(\frac{\pi\beta}{2}\right) + (\omega\tau)^{2\beta}}$$

in which ω is the angular frequency, χ_T the isothermal susceptibility, χ_S the adiabatic susceptibility and β describes the distribution of relaxation times. β was found to be similar in all cases in the range 0.82-1, indicating only a limited distribution of relaxation times.

Electron Paramagnetic Resonance (EPR)

EPR experiments, both continuous wave (CW) and pulsed time domain (TD), were performed with a Bruker Biospin ELEXSYS E-580 spectrometer operating in the X-band, using a gas-flow Helium cryostat for low-temperature experiments. 2p and Inversion Recovery ESE-detected experiments were performed. In these experiments the length of the $\pi/2$ pulse was, typically, 16 ns whereas the length of the π pulse was 32 ns. Samples were of **1** and **3** crystalline and not previously subjected to vacuum drying.

Simulation of the echo-induced EPR spectrum was done with Easyspin[6] with the following Spin Hamiltonian (SH):

$$H = \mu_B B\left\{g_\perp\left(S_X^{(1} + S_X^{(2} + S_Y^{(1} + S_Y^{(2}\right)\sin\theta + g_\parallel\left(S_Z^{(1} + S_Z^{(2}\right)\cos\theta\right\} +$$
$$A_\perp\left(S_X^{(1}I_X^{(1} + S_X^{(2}I_X^{(2} + S_Y^{(1}I_Y^{(1} + S_Y^{(2}I_Y^{(2}\right) + A_\parallel\left(S_Z^{(1}I_Z^{(1} + S_Z^{(2}I_Z^{(2}\right)$$
$$+\left\{J_X S_X^{(1}S_X^{(2} + J_Y S_Y^{(1}S_Y^{(2} + J_Z S_Z^{(1}S_Z^{(2}\right\}$$

The first term in the SH describes the Zeeman interaction of the two equivalent vanadyl spins, with respective indexes 1 and 2, θ being the angle between the applied magnetic field B direction and the vanadyl axis. The second term corresponds to the hyperfine interaction of each vanadyl spin with its nuclear spin. Parameters $g_\parallel$, $g_\perp$, $A_\parallel$ y $A_\perp$ have their usual meaning. The last term takes into account the interaction among the spins of the two equivalent vanadyl, with for Heisenberg interaction $J_X = J_Y = J_Z = J_{iso}$, for an in-plane exchange coupling $J_X = J_Y = J_{XY}$ and $J_Z = 0$, and for a dipolar interaction $J_X = J_Y = -J_D$ and $J_Z = 2J_D$.

In all simulations shown in Figs. 4 and S13-S15, the following parameters were used: $g_\parallel = 1.963$; $g_\perp = 1.99$; $A_\parallel = 425$ MHz; $A_\perp = 172$ MHz, and the value of either J_{iso}, J_{XY} or J_D was varied.

Figures

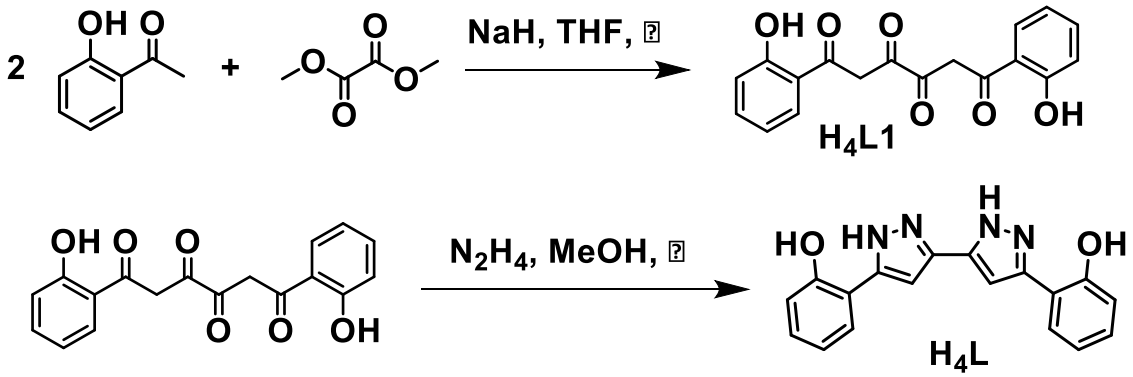

Scheme S1. Synthesis of ligands H_4L1 and H_4L.

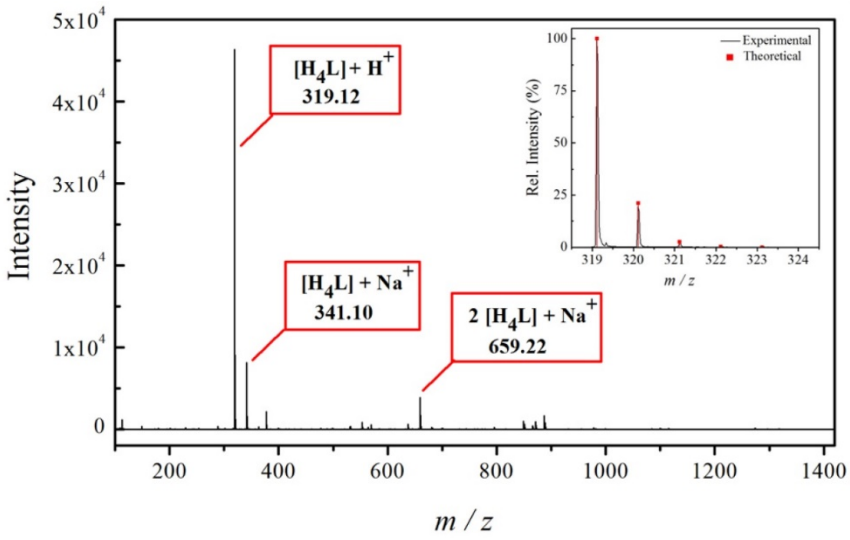

Figure S1. ESI (+) Mass Spectrogram of H_4L in solution of acetone. The inset shows the isotopic distribution of the most intense peak.

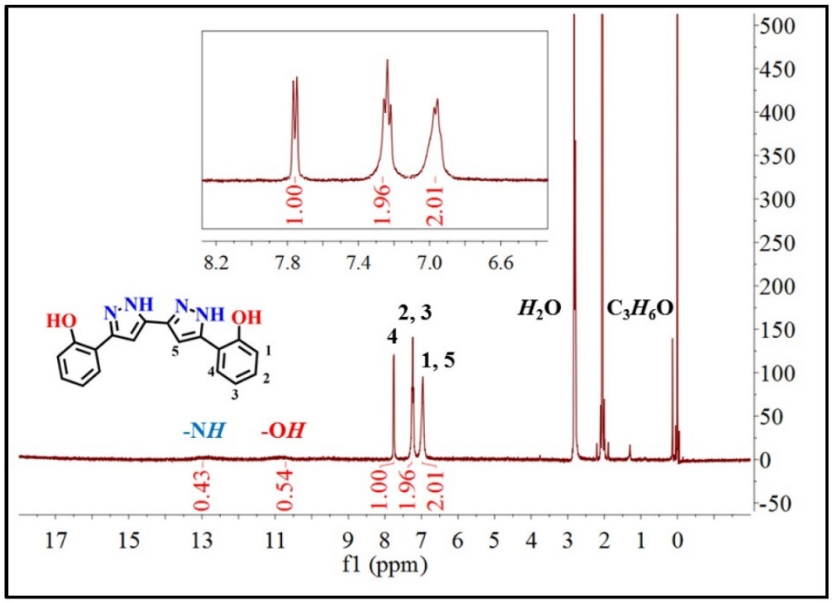

Figure S2. ^{1}H NMR spectrum of H_4L in deuterated acetone with a tentative assignment. The inset shows an expansion of the aromatic region.

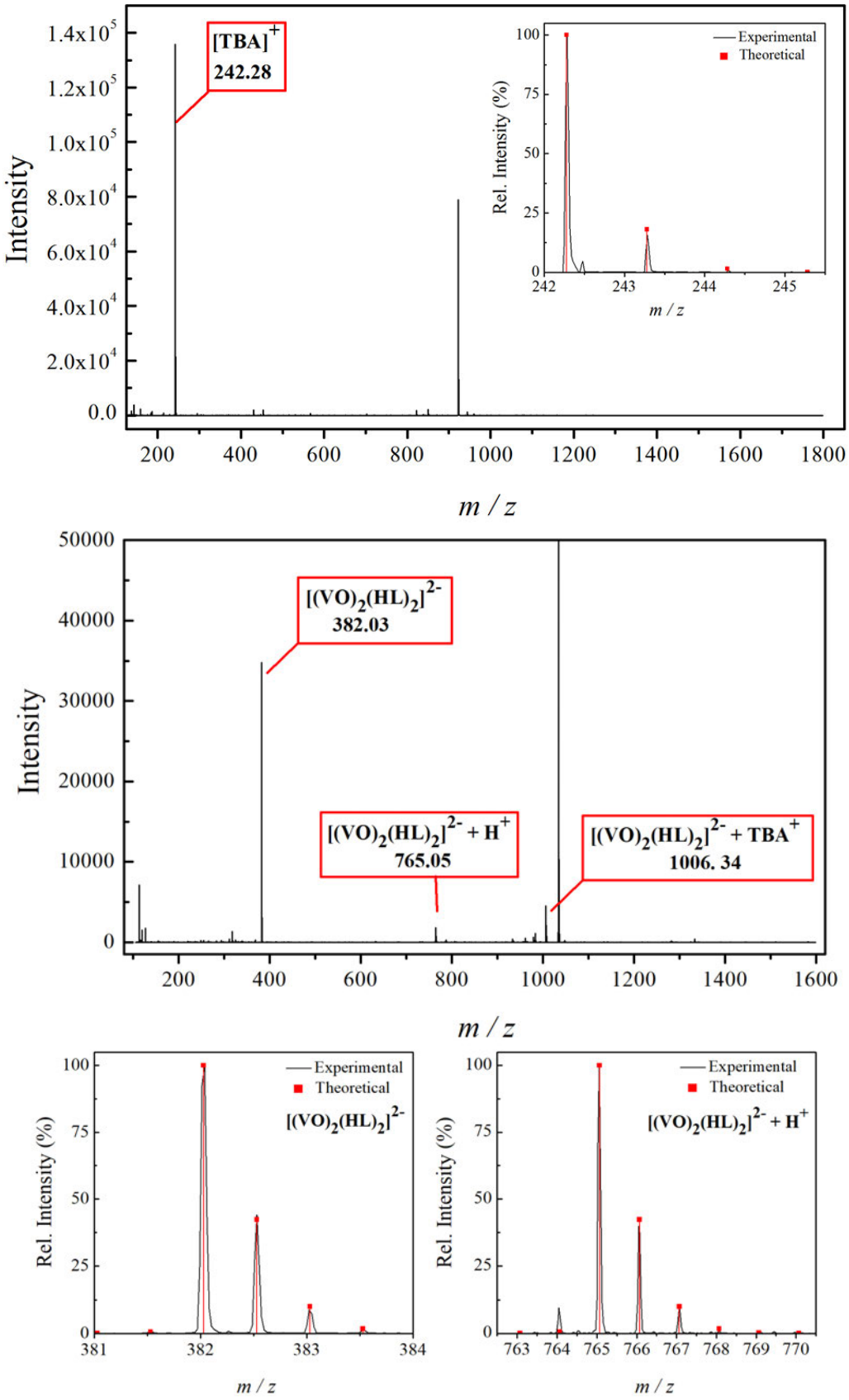

Figure S3: ESI mass spectrogram of methanol solution of compound **1**. *Top*: (+) mode with the isotopic distribution for TBA^+. *Bottom*: (-) mode with the isotopic distribution for two most abundant molecular peaks.

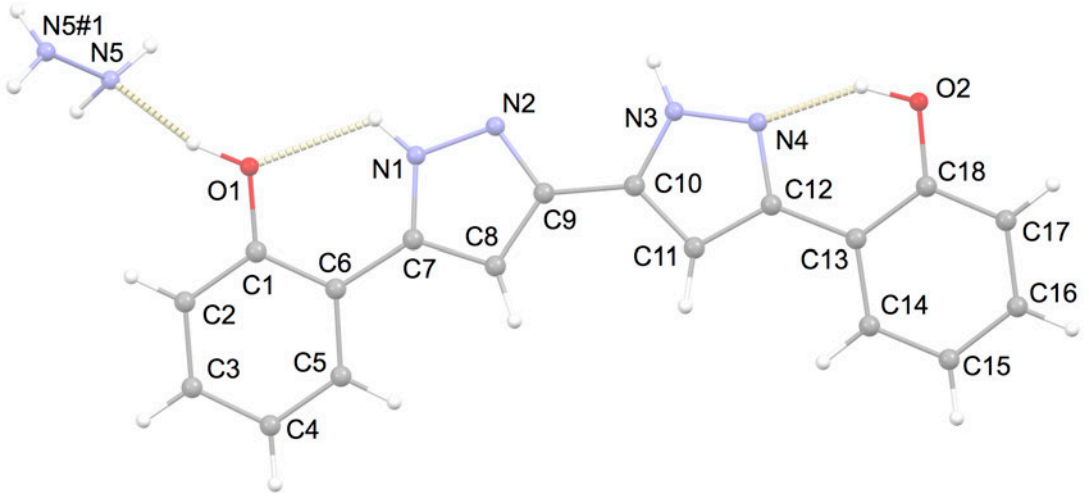

Figure S4. Labelled molecular structure of H_4L and its half molecule of hydrazine of crystallization (#1 = -x, y, 0.5-z). Hydrogen labels are omitted and hydrogen bonds are shown as yellow lines.

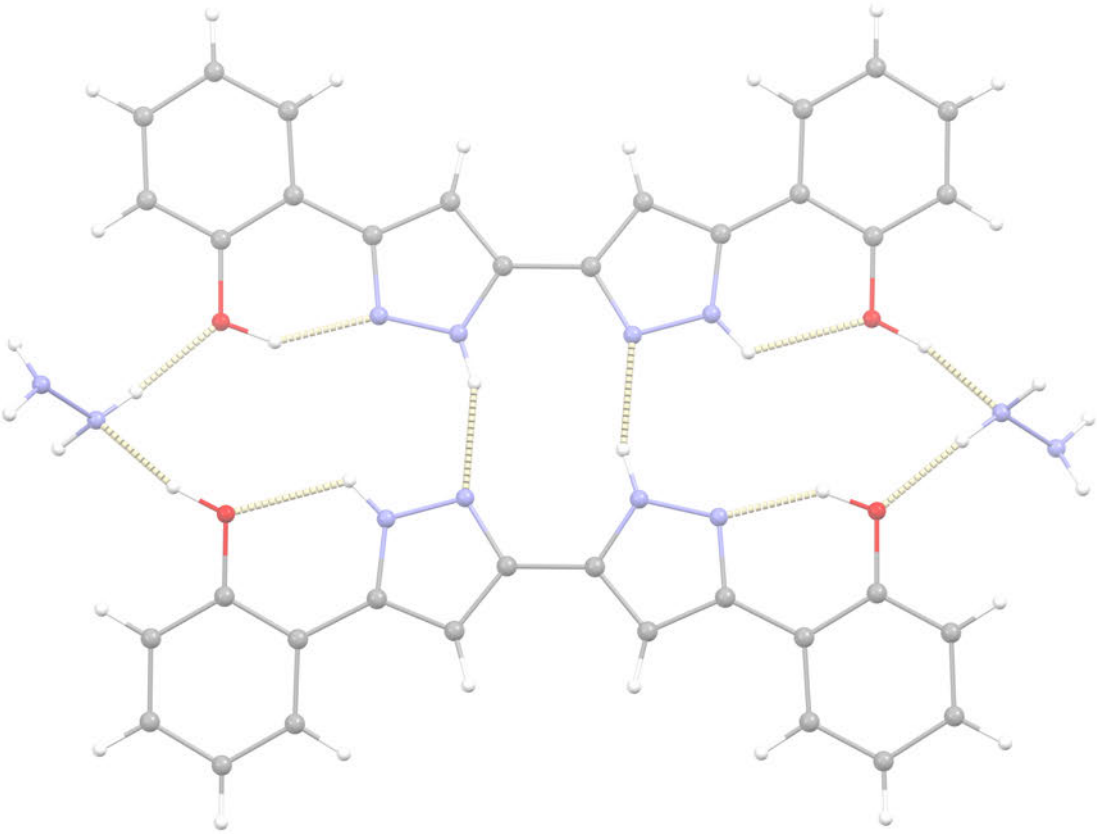

Figure S5. Representation of two molecules of H_4L, exhibiting two mutual hydrogen bonds, and two molecules of hydrazine of crystallization. Atoms colored as in Figure S4. Hydrogen bonds are shown as yellow dashed lines.

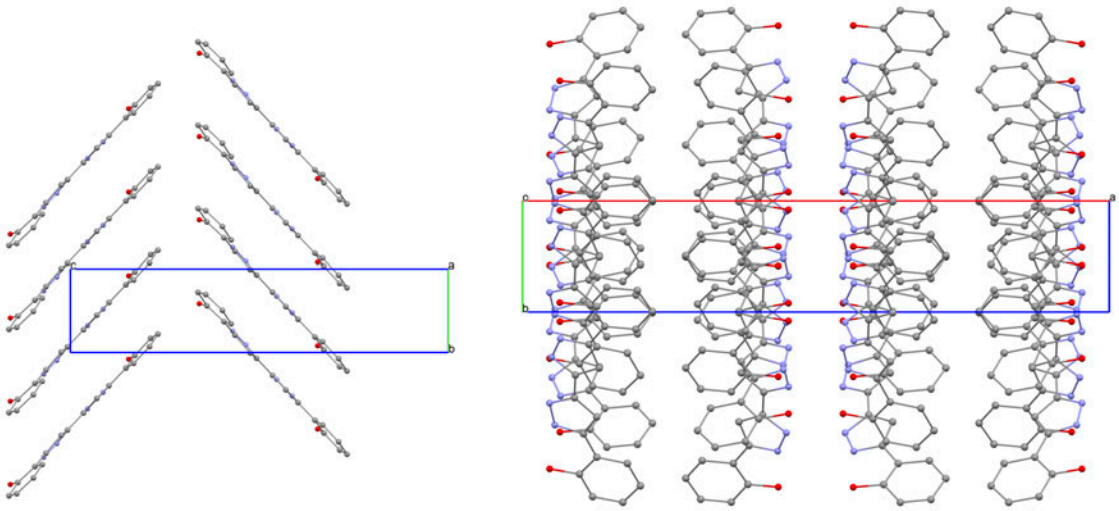

Figure S6. (left) Representation of two stacks of molecules of H_4L formed through π···π interactions, in two almost perpendicular orientations, and both running in the direction of the *c* axis. (right) Sheets of stacked molecules of H_4L lying in the *bc* plane. Hydrogens and hydrazine molecules are omitted for clarity.

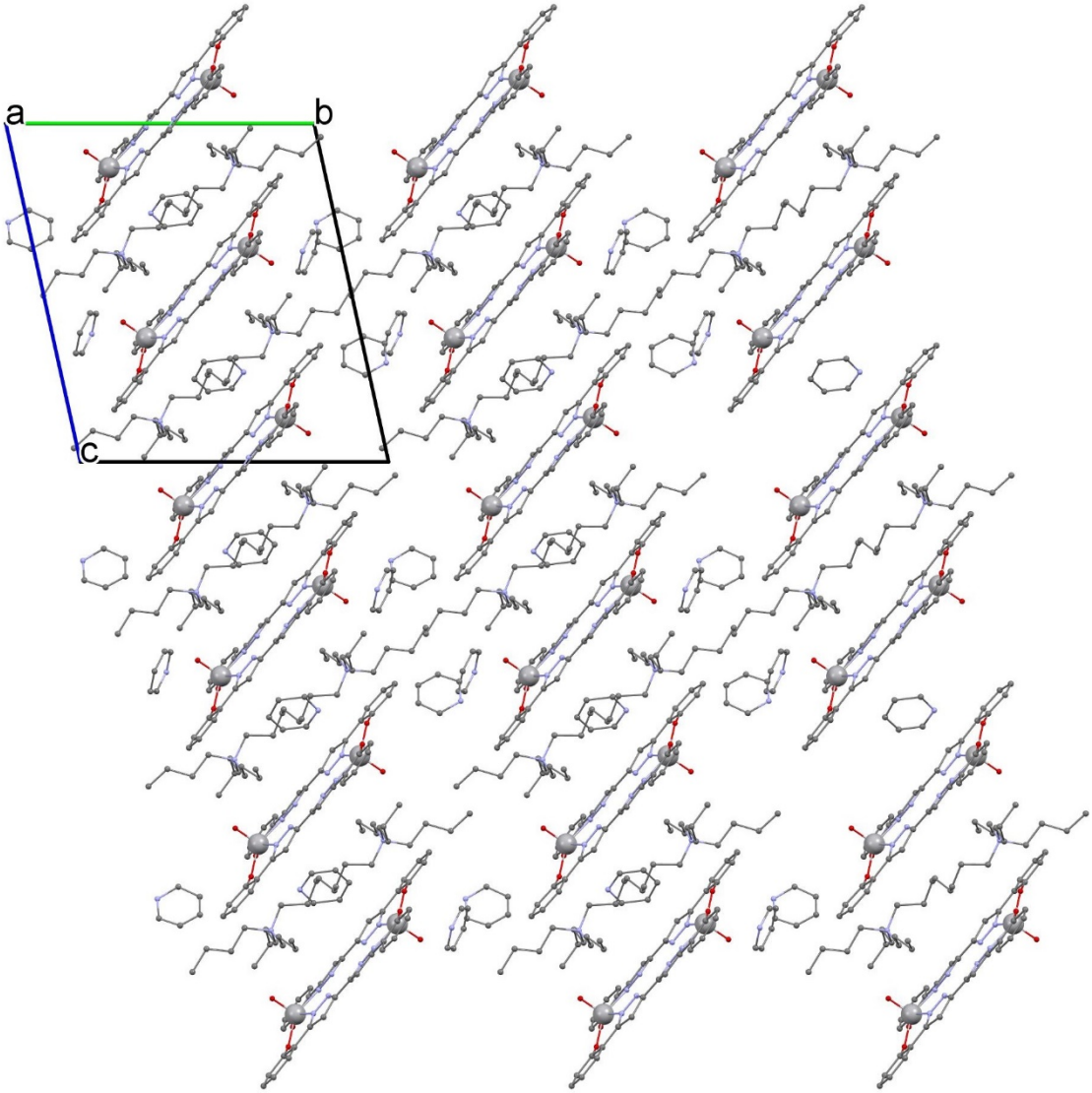

Figure S7. View of the packing within the lattice of $(Bu_4N)_2[(VO)_2(HL)_2]$ (**1**), including the solvate molecules, emphasizing the alternation of anionic complexes and cations.

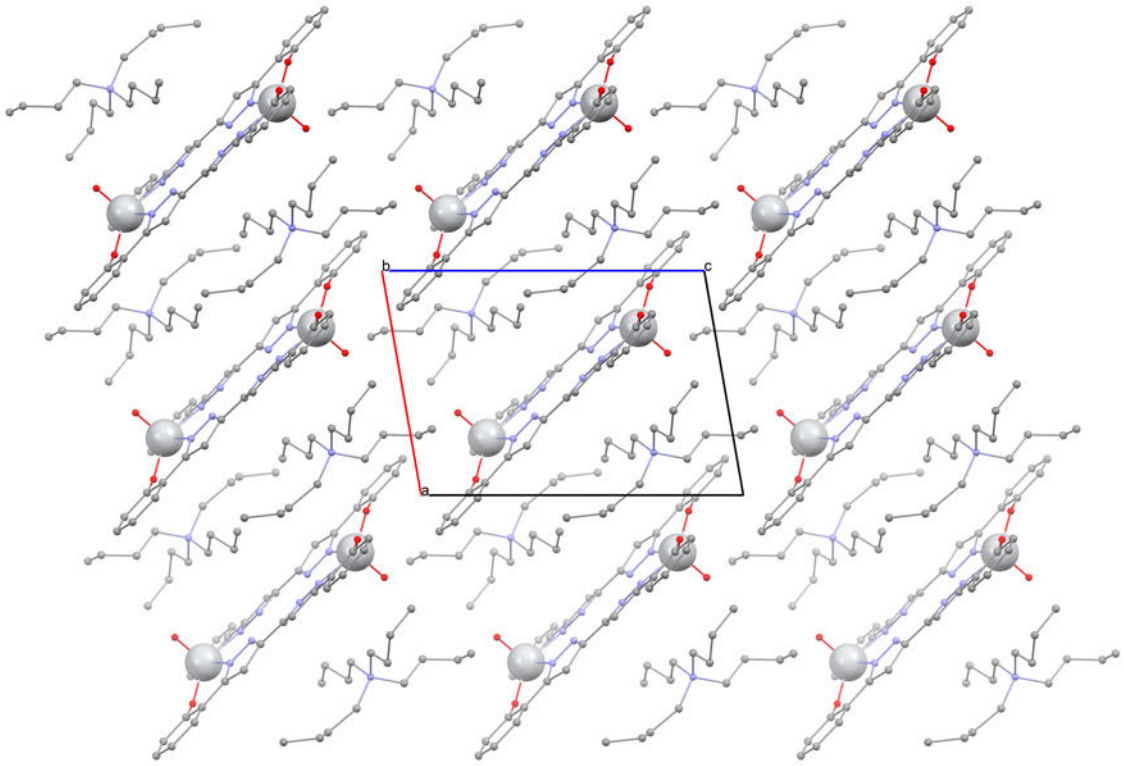

Figure S8A. View of the packing within the lattice of $(Bu_4N)_2[(TiO)_2(HL)_2]$ (**2**), emphasizing the alternation of anionic complexes and cations. Only one component of the disordered tetrabutylammonium cations is shown for clarity.

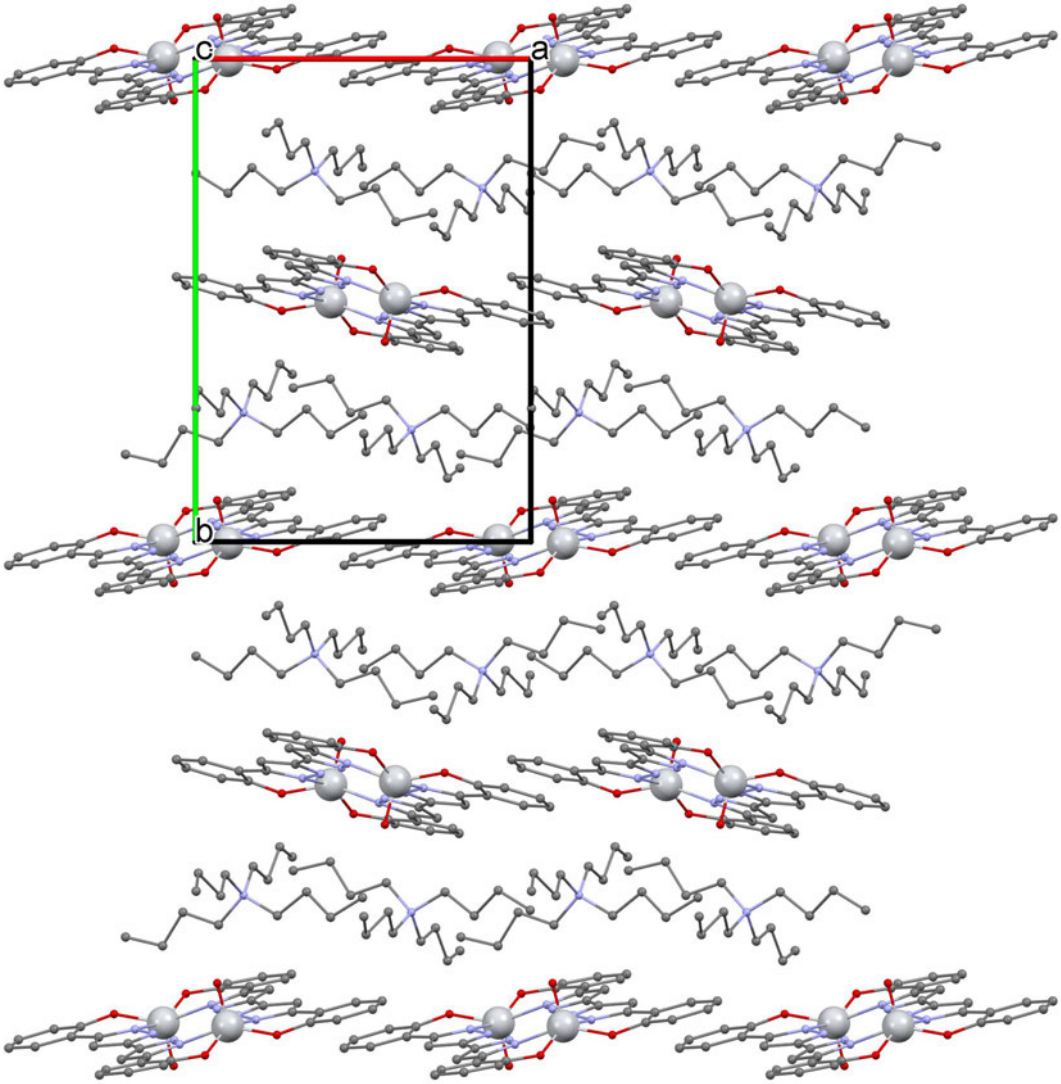

Figure S8B. View of the packing within the lattice of $(Bu_4N)_2[(TiO)_2(HL)_2]$ (**2'**), emphasizing the alternation of anionic complexes and cations.

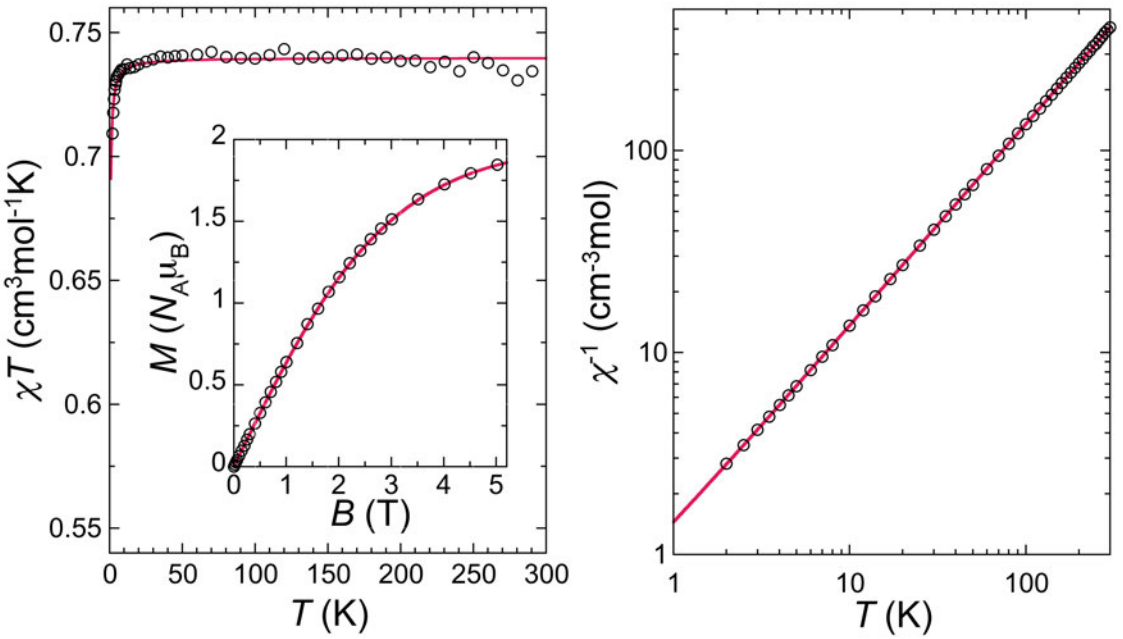

Figure S9. Left: temperature dependence of χT for **1** as derived from *dc* measurements at 0.01 T (empty symbols). The red line represents the Curie-Weiss law for C = 0.7398 cm^3mol^{-1} and θ/k_B = –0.07 K (θ = –0.048 cm^{-1}). Inset: Magnetization isotherm at 2 K for **1** with the corresponding Brillouin function for S = 1/2 and g = 1.98 depicted as red line. Right: temperature dependence of χ^{-1} highlighting the Curie-Weiss law for C = 0.7398 cm^3mol^{-1} and θ/k_B = –0.07 K (θ = –0.048 cm^{-1}, red line).

Note that a good agreement is also obtained fitting a simple model of two exchange-coupled S = 1/2 spins based on the Hamiltonian $H = -JS_1S_2$ to the experimental temperature dependence of χT. Nevertheless, the derived J/k_B = –0.270 K (J = –0.188 cm^{-1}) appears unreasonably large considering the topology of the $[(VO)_2(HL)_2]^{2-}$ complex.

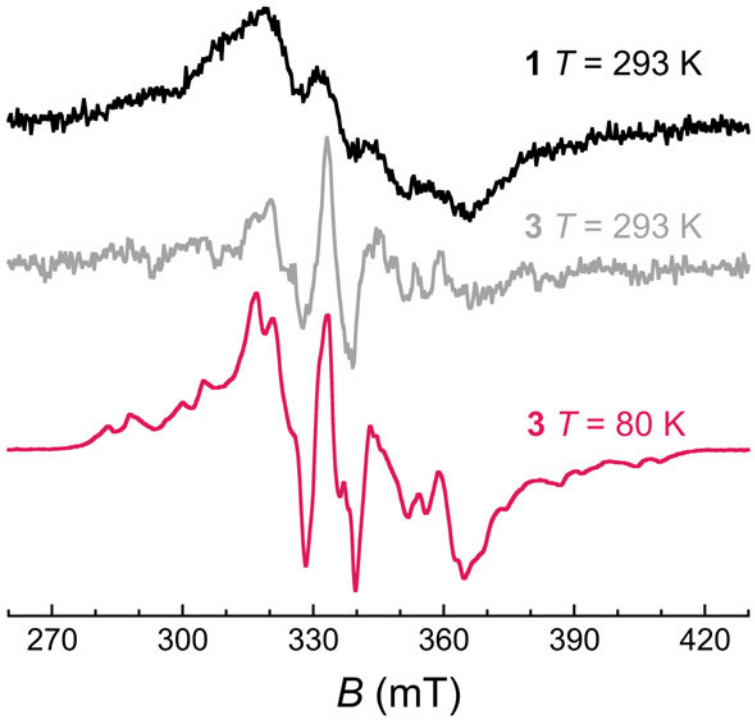

Figure S10. Comparison between the observed CW-EPR spectra of **1** and **3** at 293 K, and **3** at 80 K.

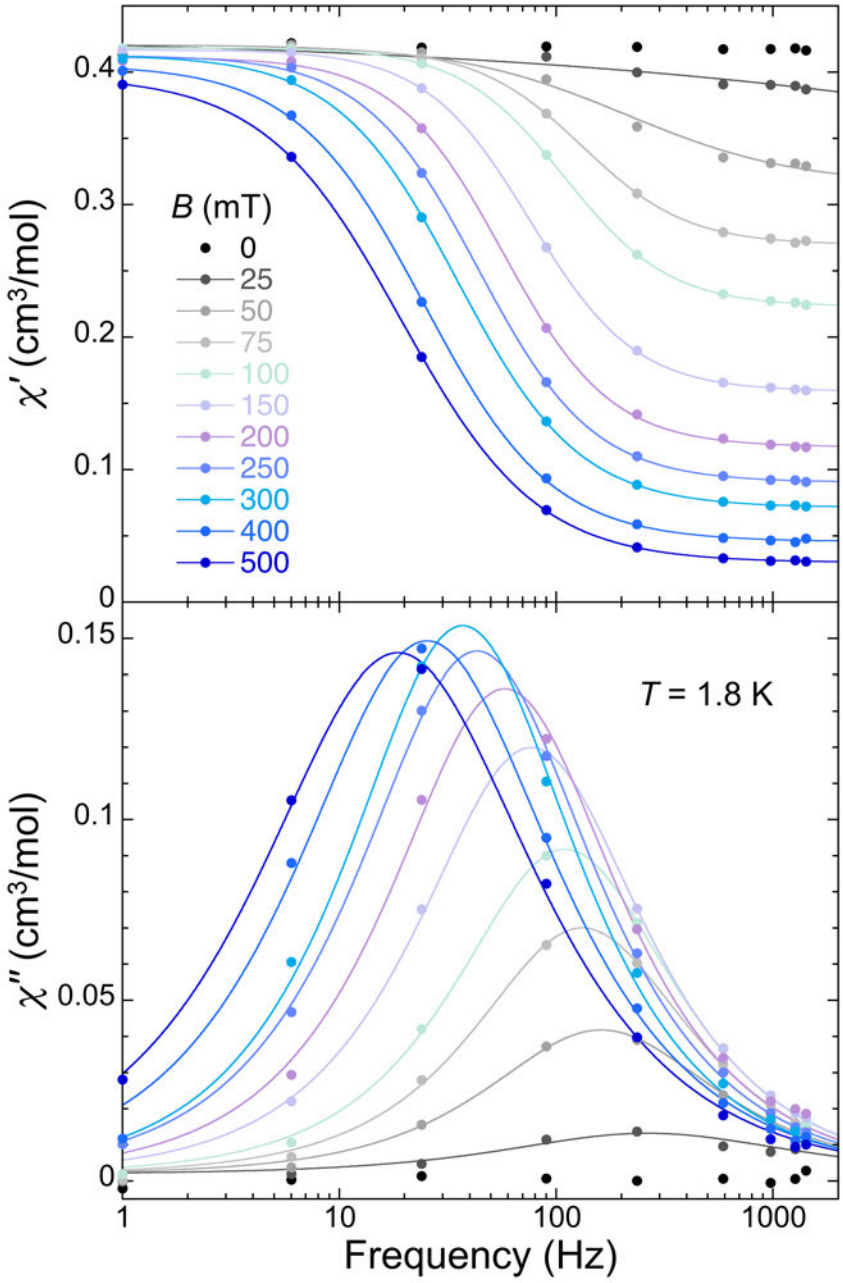

Figure S11. Frequency dependence of the in-phase (top) and out-of-phase (bottom) *ac* magnetic susceptibility of **1** at 1.8 K and increasing applied *dc* fields as indicated. Lines are fits of the experimental data to the Cole-Cole expressions for the real and imaginary susceptibility.

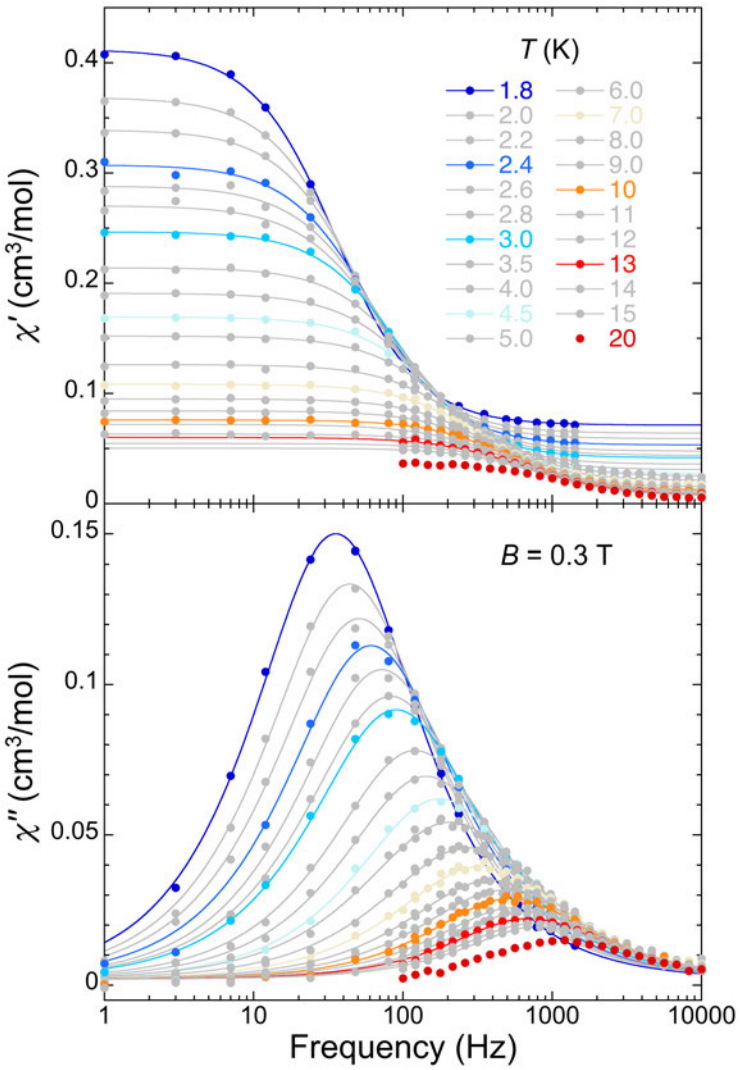

Figure S12. Frequency dependence of the in-phase (top) and out-of-phase (bottom) *ac* magnetic susceptibility of **1** at 0.3 T and increasing temperatures as indicated. Lines are fits of the experimental data to the Cole-Cole expressions for the real and imaginary susceptibility.

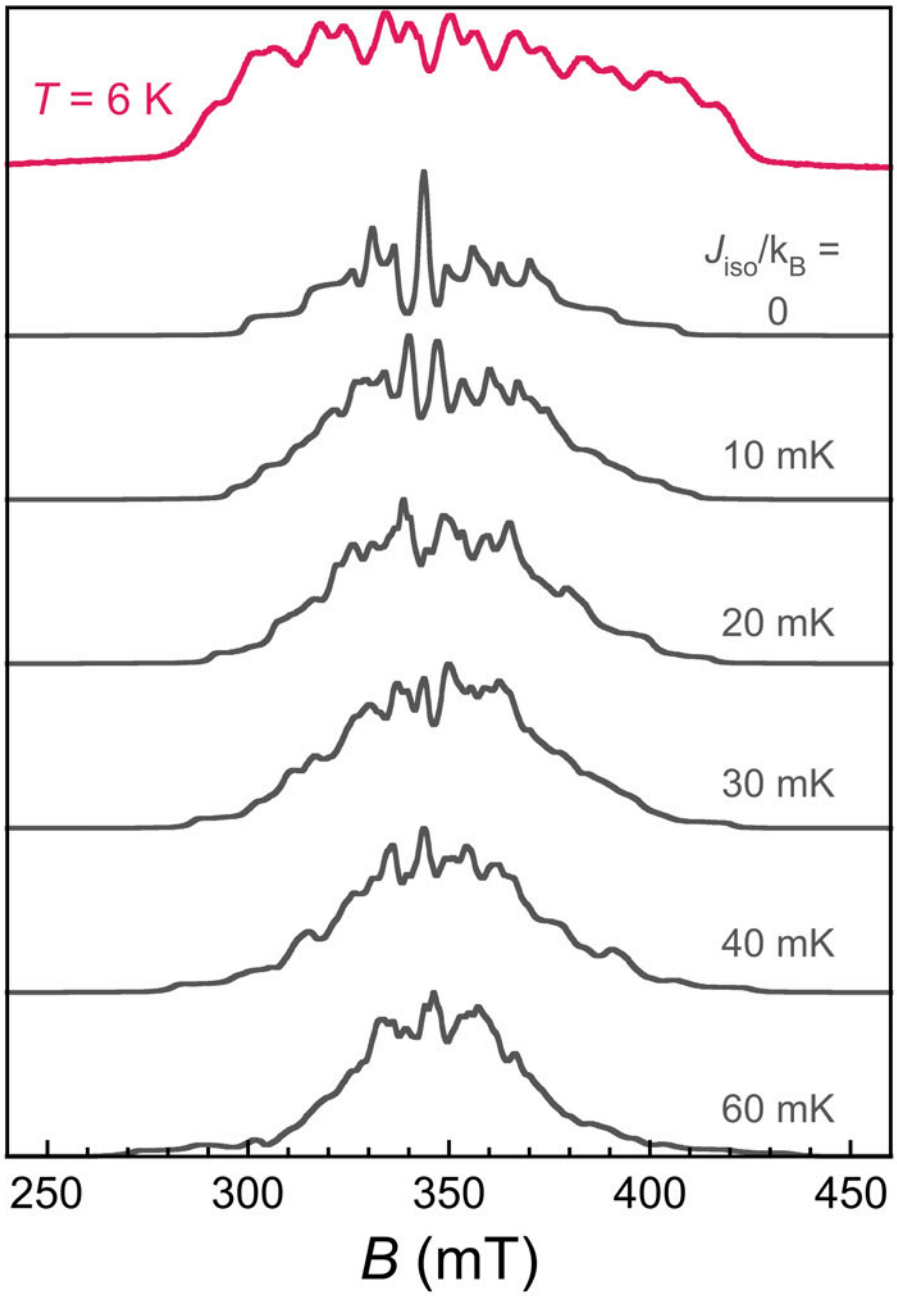

Figure S13. ESE-detected 2p EPR spectrum of **3** at 6 K (top trace) and its simulation with Easyspin[6] (top red trace) and a spin Hamiltonian contemplating two equivalent axial vanadyl spins ($g_{||}$ = 1.963; $g_{\perp}$ = 1.99; $A_{||}$ = 425 MHz; $A_{\perp}$ = 172 MHz) coupled through an isotropic Heisenberg exchange interaction J_{iso}/k_B of increasing strength.

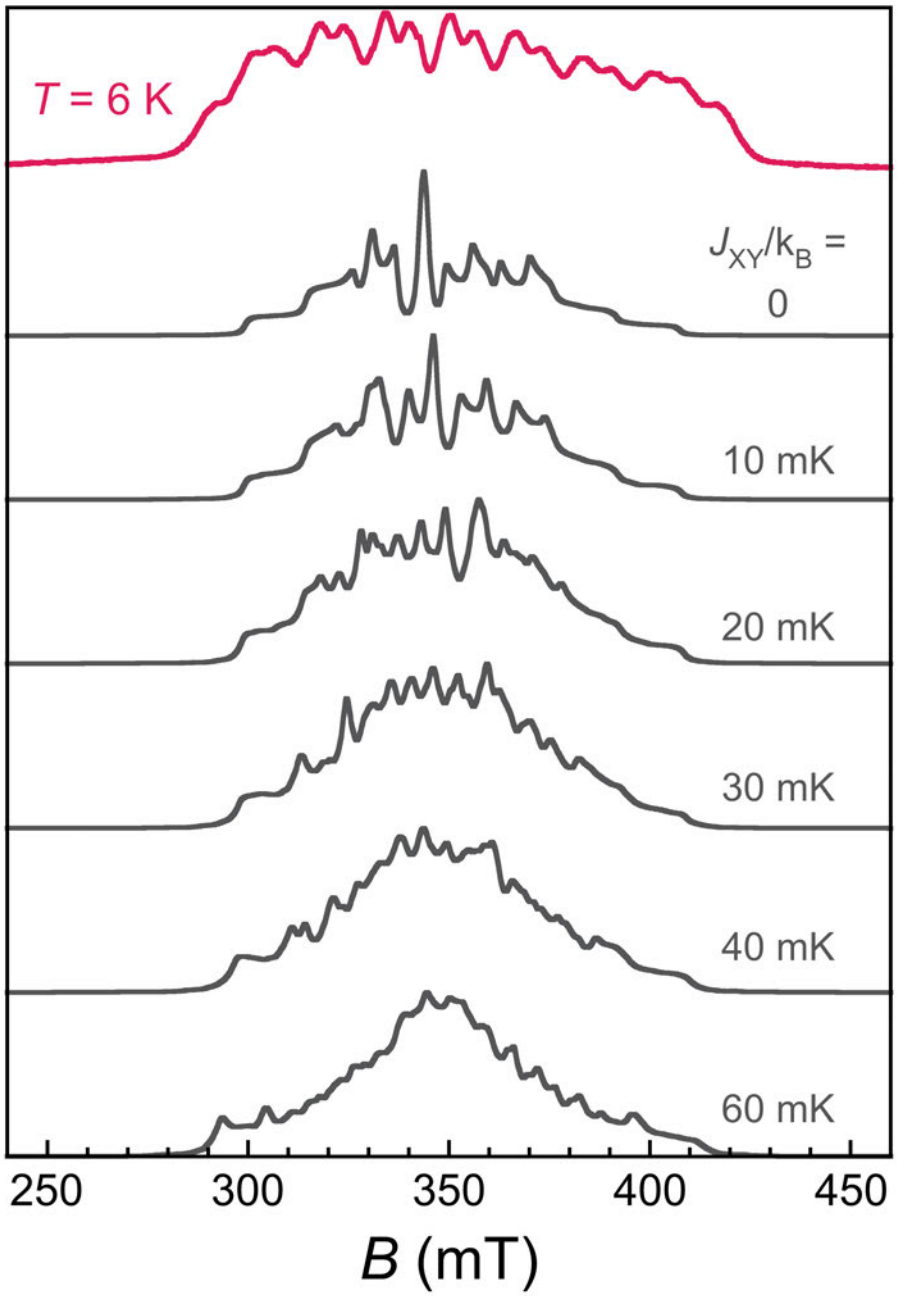

Figure S14. ESE-detected 2p EPR spectrum of **3** at 6 K (top trace) and its simulation with Easyspin[6] (top red trace) and a spin Hamiltonian contemplating two equivalent axial vanadyl spins ($g_{||}$ = 1.963; $g_{\perp}$ = 1.99; $A_{||}$ = 425 MHz; $A_{\perp}$ = 172 MHz) coupled through an in-plane exchange interaction J_{XY}/k_B of increasing strength.

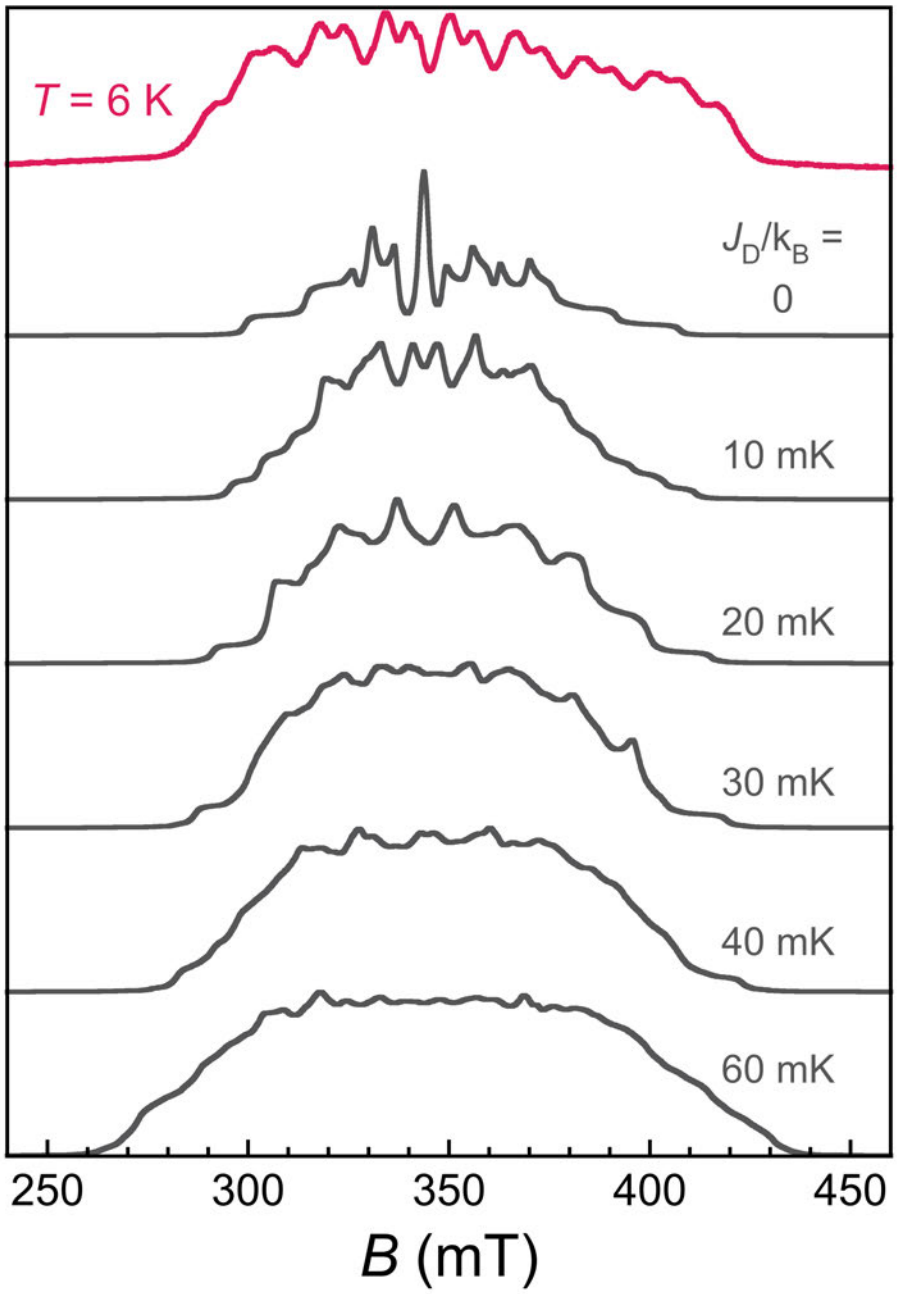

Figure S15. ESE-detected 2p EPR spectrum of **3** at 6 K (top trace) and its simulation with Easyspin[6] (top red trace) and a spin Hamiltonian contemplating two equivalent axial vanadyl spin ($g_{||}$ = 1.963; $g_{\perp}$ = 1.99; $A_{||}$ = 425 MHz; $A_{\perp}$ = 172 MHz) coupled through a dipolar interaction J_D/k_B of increasing strength.

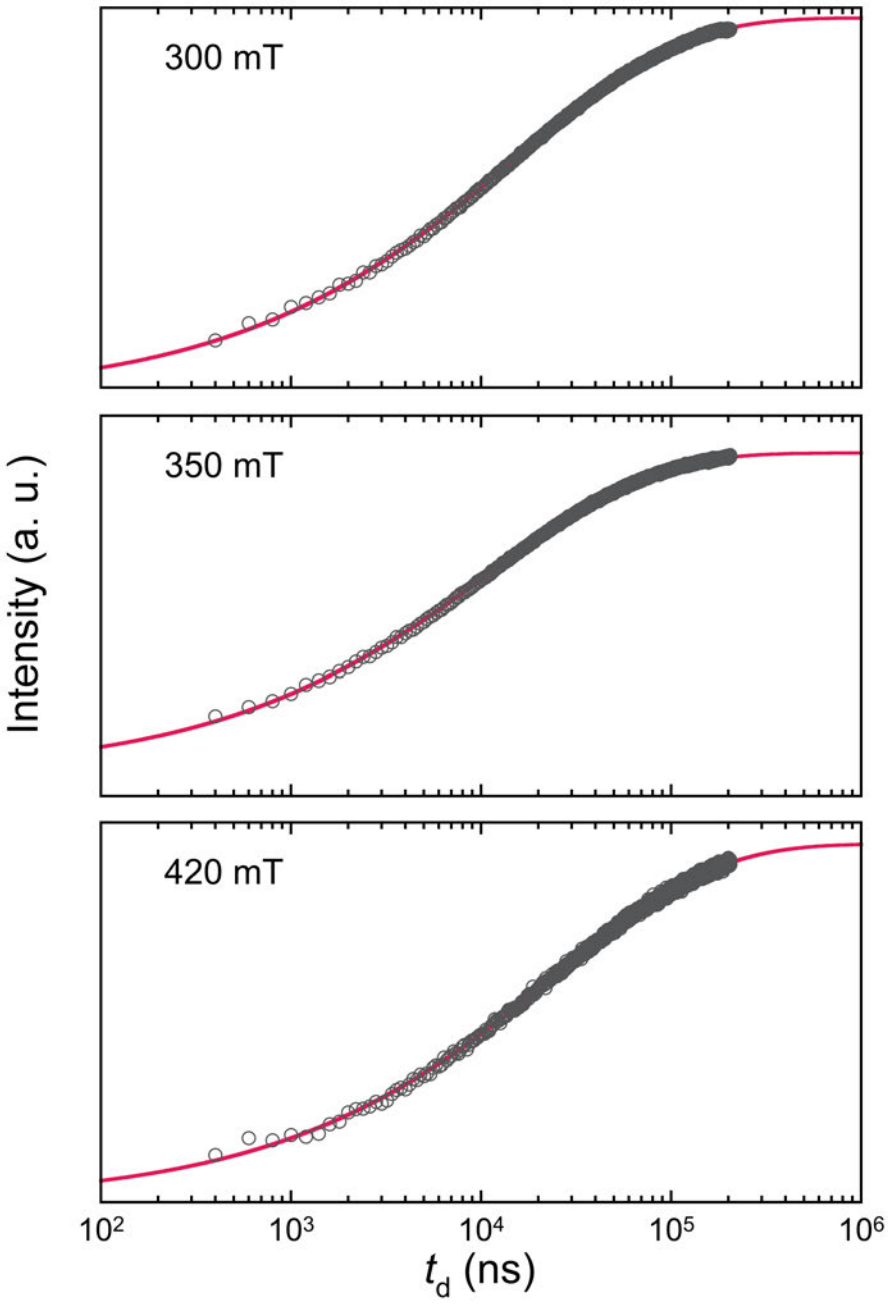

Figure S16. ESE detected Inversion Recovery as a function of delay time, t_d, for **3** at 300 350 and 420 mT (circles). Red lines correspond to a stretched exponential t_d dependence modeled by:[7]

$$y(t_d) = y_\infty - y_0 e^{-\left(t_d/\beta T_1'\right)^\beta}$$

that best fit to the data. The values of the relevant best-fit parameters are gathered in Table S1.

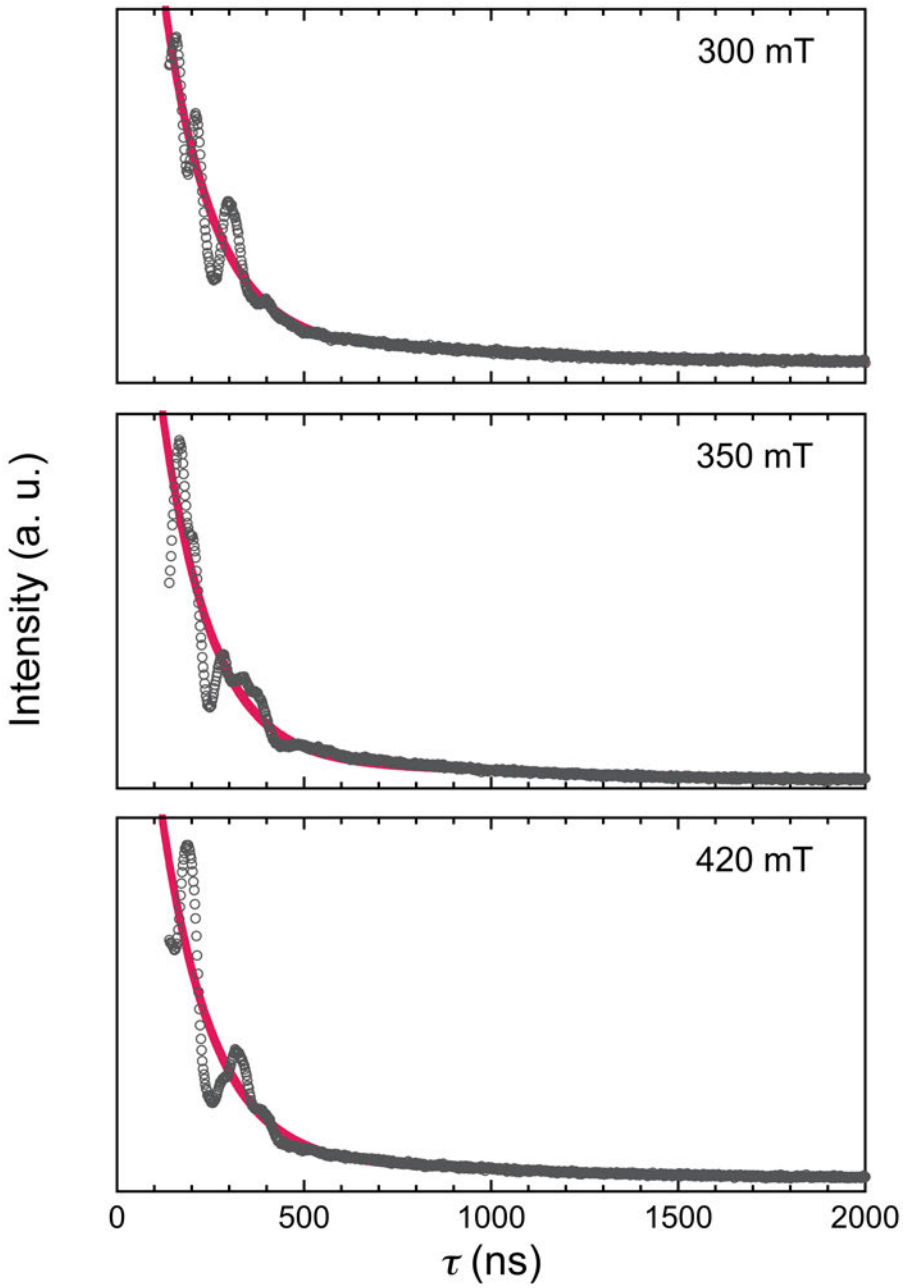

Figure S17. 2p ESE intensity as a function of inter-pulse interval, τ, for **3** at 300, 350 and 420 mT (circles). Red lines correspond to the evolution predicted with an exponential decay expressed as:

$$y(\tau) = y_0 + A_{2p} e^{-2\tau/T_M}$$

with the values of the parameters that give the best fit gathered in Table S1.

Table S4. Parameters that provide the best fits to ESE detected Inversion Recovery signals and the 2p-ESE decay for **3** measured at 6 K.

B (mT)	T_1' (μs)	β	$T_1 = T_1'/\beta$ (μs)	T_M (μs)
300	62.44 ± 0.17	0.50	125.4 ± 0.9	0.26 ± 0.01
350	45.33 ± 0.13	0.51	89.1 ± 0.6	0.26 ± 0.01
420	96.46 ± 0.74	0.51	189.5 ± 3.3	0.27 ± 0.01

References.

[1] J. Juanhuix , F. Gil-Ortiz , G. Cuní , C. Colldelram , J. Nicolás , J. Lidón , E. Boter , C. Ruget , S. Ferrer and J. Benach , *J. Synchrotron Radiat.*, 2014, **21** , 679-689

[2] G. M. Sheldrick, 2012, *SAINT and SADABS*, Bruker AXS Inc., Madison, Wisconsin, USA.

[3] Agilent (2014). *CrysAlis PRO*. Agilent Technologies Ltd, Yarnton, Oxfordshire, England.

[4] G. M. Sheldrick, *Acta Cryst. A*, 2015, **71**, 3-8.

[5] G. M. Sheldrick, *Acta Cryst. C*, 2015, **71**, 3-8.

[6] S. Stoll, and A. Schweiger, *J. Magn. Reson.*, 2006, **178**, 42

[7] expression equivalent to the conventional expression for a stretched exponential considering $T_1 = T_1'/\beta$. In the case where the stretched exponential represents a distribution of exponential decays, it has been proven that for $\beta \leq 1$, T_1 corresponds to the mean value of the relaxation times, see D.C. Johnston, *Phys. Rev. B*, 2006, **74**, 184430.